Multichannel tunneling in multiband heterostructures: Heavy-hole and light-hole transmission properties

L. Diago-Cisneros,[1,*] H. Rodríguez-Coppola,[1] R. Pérez-Álvarez,[2] and P. Pereyra[3,4,†]
[1]*Departamento de Física Aplicada, Universidad de La Habana, Codigo Postal 10400, La Habana, Cuba*
[2]*Departamento de Física Teórica, Universidad de La Habana, Codigo Postal 10400, La Habana, Cuba*
[3]*Area de Física Teórica y Materia Condensada, UAM-Azcapotzalco, Codigo Postal 02200 México Distrito Federal, Mexico*
[4]*The Abdus Salam International Centre for Theoretical Physics, Trieste, Italy*
(Received 1 December 2005; revised manuscript received 16 March 2006; published 13 July 2006)

Based on the standard multiband Hamiltonians, the quadratic eigenvalue problem method and the multichannel transfer matrix technique, we develop a general approach to study multichannel-multiband transport properties through multilayered systems. In this approach we deal simultaneously with all the accessible physical channels. We are thus able to distinguish and to calculate transmission amplitudes, t_{ij}, for each pair j,i of incoming and outgoing propagating modes. We apply this approach to study hole tunneling through single-barrier and multiple-barrier semiconductor heterostructures, modeled by a zero-biased (4×4) Kohn-Luttinger Hamiltonian. We calculate transmission coefficients and the Landauer conductance for systems with coupled and uncoupled channels. A very good agreement with experimental results is found when applied to double barrier resonant tunneling systems. We find interesting underbarrier interference and resonance effects.

DOI: 10.1103/PhysRevB.74.045308 PACS number(s): 73.43.Jn, 74.50.+r, 03.65.Nk, 31.10.+z

I. INTRODUCTION

The transport and tunneling processes of electrons and holes through semiconductor heterostructures are important topics in solid state and condensed matter physics. Compared with electrons, holes, and the physical structures where these particles are important charge carriers have been much less studied because of the mathematical complexity characterizing the theoretical approaches. The lack of interest on a complete characterization of holes passing through semiconductor systems was, very likely, based on the assumption that the characteristic times of optoelectronic devices, in which electrons and holes participate, is limited by the last ones because of their larger effective mass. Nevertheless, transmission time experiments with GaAs-AlAs superlattices[1] have shown that sequential resonant tunneling from *hh* into *lh* as well as from *hh* into higher hh subbands occurs faster than transport due to nonresonant tunneling of electrons, in spite of their mass.

It is known that while the weakly coupled multimode electron tunneling can, in principle, be properly described within a one-dimensional (1D) (single-mode) approximation (implicit in the WKB, transference Hamiltonian,[2] Wannier[3] and Wigner[4] functions, and the 1D transfer matrix[5,6] approaches), the strongly coupled multimode (multichannel) systems, in general, and the strongly mixed nonparabolic band states, in particular, cannot. Multimode problems have been considered with relative success in the framework of tight-binding approximations[7] (for valence bands), and the $\boldsymbol{k}\cdot\boldsymbol{p}$ approach[8,9] for valence and conduction band mixing.[10] In the tight binding and $\boldsymbol{k}\cdot\boldsymbol{p}$ approaches, some effective $N\times N$ Hamiltonians[7–10] are built on and, eventually, the solutions described within the envelope function approximation (EFA). Even though these solutions are multicomponent wave functions, it is usual to cancel arbitrarily all components but one of them,[11–15] to determine transmission coefficients. Besides this, it is also usual, after block diagonalizing, to work in reduced Hilbert spaces,[15,16] which, taken separately, do not fulfill all the physical symmetries of the whole Hilbert space.[17] Furthermore, transitions between states of different Kramer sign cannot be described in these reduced Hilbert spaces. It is clear then, that following the actual one-component flux approaches and using valence band states with undefined projection of the total angular momentum (as is the case for the 2×2 models), important physical information is lost. Hence, the one-component flux description for a transport process characterized by mixed-multicomponent flux is unreliable. We propose here an alternative approach where all the propagating modes are taken into account jointly and simultaneously, and a multicomponent description of transmission amplitudes is carried out in a natural way. In this paper we combine the effective $N\times N$ Hamiltonians of the $\boldsymbol{k}\cdot\boldsymbol{p}$ approach with the multichannel (multimode) transfer matrix approach.[18–20] To solve the second order differential equation associated to N-fold Kohn-Luttinger-type Hamiltonians and to obtain the momentum eigenvalues, we follow the quadratic eigenvalue problem (QEP) method employed by Tisseur and Meerbergen in Ref. 21. We show that using an orthonormal basis derived from QEP, the important flux conservation requirement is rigorously satisfied. Therefore, it is not necessary to introduce arbitrary factors to normalize transmission coefficients.[12,16,22] For calculation of transport properties of multichannel-multilayered systems, we employ the finite periodic systems theory.[23]

On the experimental side, some interesting transport properties and features, such as the strong κ_{T} (the in plane quasimomentum) dependence of the resonant hole transmission coefficients, have been reported recently.[11–15] We are mainly interested here on the *transmission amplitudes matrix*, which like the scattering matrix S contains entire information on the scattering process described by the model Hamiltonian. Once the transmission amplitudes are obtained, one can readily determine transmission coefficients $T_{i,j}$, and specific transport properties, such as the channel interference characteris-

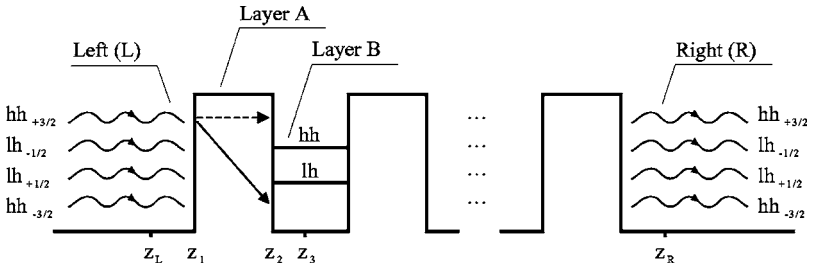

FIG. 1. Schematic representation of multichannel *hh* and *lh* transport processes through a GaAs-cladding layer $(L)/(\mathrm{AlAs/GaAs})^n/$ GaAs-cladding layer (R) superlattice in the absence of external fields or strains. In the cladding layers, *hh* and *lh* modes mix due to the $\boldsymbol{k}\cdot\boldsymbol{p}$ interaction. By complex-momentum valued states, holes propagate through the classically forbidden *Layer A, via* the threshold effect, activating a closed path. The dashed and solid arrow will be used below to represent direct and crossed transitions, respectively. In *Layer B*, holes are allowed to perform a resonant transport at energies of the quasibound states in the well. As we increase the energy and surmount the channel threshold, we increase the number of allowed propagating modes.

tics, and global quantities such as the Landauer conductance, as functions of the incoming Fermi energy and the heterostructure parameters.

In Sec. II, assuming an arbitrary $N\times N$ Hamiltonian, we outline the principal theoretical methods contained in the present approach. Basically, the so-called quadratic eigenvalue problem (QEP)[21] method (adjusted to obtain the momentum eigenvalues and an orthonormal basis) and the transfer matrix method brought in to establish an easy relation with the scattering amplitudes matrices. This approach will be applied, in Sec. III, to study hole-transport properties through III-V semiconductor heterostructures described by the (4×4) Kohn-Luttinger (KL) model.[24] Note that the hole tunneling through III-V semiconductor heterostructures is beset also by the fact that most, though not all, of the descriptions of hole states have been obtained within the (2×2) Kohn-Luttinger (KL) model that limits the possibility of observing transition probabilities between different angular momentum projection states and transmission between hole states with different Kramer's sign (under time reversal symmetry operation). In Sec. IV, we will present several transmission coefficient results exhibiting among other features, the mixing of light holes (*lh*) and heavy holes (*hh*).[9,15,16,24] We choose these quasiparticles not only because they were much less studied than the electrons, but also because they constitute intrinsically a multichannel physical system, whose relevance has been suggested in the performance of optoelectronic semiconductor devices.[1,25] Finally, in Sec. V we sum up and conclude.

II. THE MULTICOMPONENT SCATTERING APPROACH

The bare bones of our approach, that will be detailed in the next subsections, are the following: We assume a system, like the one shown in Fig. 1, with translational invariance in the transverse plane, described by

$$\hat{\boldsymbol{H}}(z)\boldsymbol{F}(z)=\boldsymbol{\varepsilon}\boldsymbol{F}(z), \tag{1}$$

where the spin-dependent $N\times N$ Hamiltonian $\hat{\boldsymbol{H}}(z)$, invariant to time reversal and space inversion,[26] complies with physical systems of sectionally constant potentials in the growing direction. To obtain the solutions

$$\boldsymbol{F}(z)=\sum_{j=1}^{2N} c_j\boldsymbol{\psi}_j e^{iq_j z}=\sum_{j=1}^{2N} c_j\boldsymbol{F}_j(z), \tag{2}$$

and particularly the eigenvalues q_j and the eigenvectors $\boldsymbol{\psi}_j$, we use the linearized QEP that will be explained below. Once these quantities are known and an orthonormal basis is obtained, we determine the transfer matrices $\boldsymbol{M}_{fd}(z_\mathrm{R},z_\mathrm{L})$ (relating functions and their derivatives at z_R and z_L) and $\boldsymbol{M}_{sv}(z_\mathrm{R},z_\mathrm{L})$ (relating state vectors in the propagating mode representation also at z_R and z_L). We then use the well-known relations between $\boldsymbol{M}_{sv}$ and the scattering amplitudes r and t to calculate the relevant transport theory quantities.

A. The quadratic eigenvalue problem (QEP) and orthonormalization criterium

In the actual theoretical calculations dealing with multiband $\boldsymbol{k}\cdot\boldsymbol{p}$ Hamiltonians for sectionally constant potentials, it is not usual to consider a complete set of *orthonormal* basis functions, instead the basis set of functions is normalized to Dirac's delta function in the configuration space[7–10] and arbitrary unitary conditions to the incident flux are enforced,[11–15] with complementary normalization constants for the transmission coefficients.[12,22]

The eigenvalue equation (1) for a multicomponent system with translation symmetry in the transverse $[x,y]$ plane can be written in the form

$$\frac{d}{dz}\left[\boldsymbol{B}(z)\frac{d\boldsymbol{F}(z)}{dz}+\boldsymbol{P}(z)\boldsymbol{F}(z)\right]+\boldsymbol{Y}(z)\frac{d\boldsymbol{F}(z)}{dz}+\boldsymbol{W}(z)\boldsymbol{F}(z)=\boldsymbol{O}_\mathrm{N}, \tag{3}$$

where $\boldsymbol{B}(z)$ and $\boldsymbol{W}(z)$ are, in general, $(N\times N)$ Hermitian matrices and $\boldsymbol{Y}(z)=-\boldsymbol{P}^\dagger(z)$.

Assuming a solution like $\boldsymbol{\psi}e^{iqz}$, with q a real or complex scalar and $\boldsymbol{\psi}$ is a $(N\times 1)$ spinor, we obtain the following *quadratic eigenvalue problem*:

$$\mathbb{Q}(q)=\{q^2\mathbb{M}+q\mathbb{C}+\mathbb{K}\}\boldsymbol{\psi}=\boldsymbol{O}_\mathrm{N}, \tag{4}$$

whose solutions result in the eigenvalues q_j and the eigenvectors $\boldsymbol{\psi}_j$. The matrix coefficients in this equation bear a simple relation with those in Eq. (3). In the case discussed in

Sec. IV, $\mathbb{M}=-\boldsymbol{B}$, $\mathbb{C}=2i\boldsymbol{P}$, and $\mathbb{K}=\boldsymbol{W}$. The specific symmetries of these coefficients determine the method to follow in each case. A summary of the possible QEP's problems can be found in Table 1 of Ref. 21. We will focus our attention on a case where matrices $\mathbb{M}$, $\mathbb{C}$, and $\mathbb{K}$ are $(N\times N)$ Hermitian matrices and the q_j are all different real or complex numbers. Complex eigenvalues q_j occur together with their complex conjugated q_j^*, while the real eigenvalues q_j occur together with their symmetric $-q_j$. In the problem that will be discussed below, an equation like (4) is obtained for each layer of the heterostructure.

Following Ref. 21, we linearize the QEP to get finally the associated standard eigenvalue problem (SEP), with the same eigenvalues as the QEP. In this linearization process, we derive the orthonormality conditions for the eigenvectors of the QEP, namely:

$$\boldsymbol{\psi}_k^\dagger[q_j\boldsymbol{I}_N - q_k^*\mathbb{K} + q_k^*q_j\mathbb{C}]\boldsymbol{\psi}_j = \boldsymbol{\psi}_k^\dagger\boldsymbol{L}^{kj}\boldsymbol{\psi}_j = q_k\delta_{kj}, \tag{5a}$$

$$\boldsymbol{\psi}_k^\dagger[\boldsymbol{I}_N + q_k^*q_j\mathbb{M}]\boldsymbol{\psi}_j = \boldsymbol{\psi}_k^\dagger\boldsymbol{D}^{kj}\boldsymbol{\psi}_j = \delta_{kj}. \tag{5b}$$

For real eigenvalues, the orthonormality condition can be written as

$$\boldsymbol{\psi}_k^\dagger[(q_k+q_j)\boldsymbol{B} + 2i\boldsymbol{P}]\boldsymbol{\psi}_j = \boldsymbol{\psi}_k^\dagger\boldsymbol{R}^{kj}\boldsymbol{\psi}_j = \delta_{kj}. \tag{5c}$$

In the numerical calculations of Sec. IV, we follow the Gram-Schmidt procedure to orthonormalize the basis functions, using the weight function $\boldsymbol{D}^{kj}$ in Eq. (5b).

Finally it is important to emphasize that using this orthonormalized basis, the scattering matrix satisfies the usual unitarity condition:

$$\boldsymbol{S}^\dagger\boldsymbol{S} = \boldsymbol{I}_N. \tag{6}$$

We will refer again to this fundamental property at the end of Sec. II C.

B. The N-component Hamiltonian and the transfer matrix formalism

To introduce the transfer matrices, let us now define the vector

$$\boldsymbol{\Psi}(z) = \begin{pmatrix} \boldsymbol{F}(z) \\ \boldsymbol{F}'(z) \end{pmatrix}, \tag{7}$$

which includes the wave vectors and their derivatives, and the $(2N\times 1)$ state vector

$$\boldsymbol{\Phi}(z) = \begin{pmatrix} \boldsymbol{a} & 0 \\ 0 & \boldsymbol{b} \end{pmatrix}\begin{pmatrix} \vec{\boldsymbol{\varphi}}(z) \\ \overleftarrow{\boldsymbol{\varphi}}(z) \end{pmatrix}. \tag{8}$$

Here $\boldsymbol{a}$ and $\boldsymbol{b}$ are $N\times N$ diagonal coefficient matrices, $\vec{\boldsymbol{\varphi}}(z)$ and $\overleftarrow{\boldsymbol{\varphi}}(z)$ N-dimensional vectors, whose elements describe a propagating or evanescent mode, depending on the energy.

Based on these definitions, it is possible to establish between $\boldsymbol{\psi}$ and $\boldsymbol{\Phi}$ the important relation

$$\boldsymbol{\Psi}(z) = \boldsymbol{\mathcal{N}}\boldsymbol{\Phi}(z). \tag{9}$$

The matrix $\boldsymbol{\mathcal{N}}$ depends upon the specific N-component Hamiltonian. The vectors $\boldsymbol{\psi}(z_L)$ and $\boldsymbol{\psi}(z_R)$, at any two points z_L and z_R of the heterostructure, are related by

$$\boldsymbol{\Psi}(z_R) = \boldsymbol{M}_{fd}(z_R,z_L)\boldsymbol{\Psi}(z_L). \tag{10}$$

Similarly, while describing the states using transfer matrices one has

$$\boldsymbol{\Phi}(z_R) = \boldsymbol{M}_{sv}(z_R,z_L)\boldsymbol{\Phi}(z_L). \tag{11}$$

$\boldsymbol{M}_{fd}$ and $\boldsymbol{M}_{sv}$ are, respectively, the first and second kind transfer matrices. The subscripts fd and sv stand because these matrices connect wave functions and their derivatives, in one case, and state vectors in the other. These matrices satisfy the relevant physical properties and symmetries of the Hamiltonian, such as flux conservation $j(z_L)=j(z_R)$; time reversal, spin rotation, and space inversion invariance.[17,27] In principle all transfer matrices can be obtained using the transfer-matrix multiplicative property, however, it is frequent to find, evaluating transfer matrices $\boldsymbol{M}_{fd}$, numerical instabilities which lead to introducing *ad hoc* calculation algorithms.

Using Eqs. (7)–(11), we obtain the crucial transformation

$$\boldsymbol{M}_{sv}(z_R,z_L) = \boldsymbol{\mathcal{N}}^{-1}\boldsymbol{M}_{fd}(z_R,z_L)\boldsymbol{\mathcal{N}}, \tag{12}$$

which relates the two types of transfer matrices, and opens the possibility of evaluating the scattering amplitudes. It is well-known from the scattering approach the relation between the transfer matrix $\boldsymbol{M}_{sv}$ and the scattering matrix S. In the next subsection we summarize some of these relations and the relevant physical quantities defined in terms of the scattering amplitudes.

C. The M_{sv} transfer matrix and the scattering amplitudes

Given the transfer matrix M_{sv} and the scattering matrix S definitions

$$\begin{pmatrix} \vec{\boldsymbol{\varphi}}(z_R) \\ \overleftarrow{\boldsymbol{\varphi}}(z_R) \end{pmatrix} = \boldsymbol{M}_{sv}\begin{pmatrix} \vec{\boldsymbol{\varphi}}(z_L) \\ \overleftarrow{\boldsymbol{\varphi}}(z_L) \end{pmatrix} = \begin{pmatrix} \boldsymbol{\alpha} & \boldsymbol{\beta} \\ \boldsymbol{\gamma} & \boldsymbol{\delta} \end{pmatrix}\begin{pmatrix} \vec{\boldsymbol{\varphi}}(z_L) \\ \overleftarrow{\boldsymbol{\varphi}}(z_L) \end{pmatrix} \tag{13}$$

and

$$\begin{pmatrix} \overleftarrow{\boldsymbol{\varphi}}(z_L) \\ \vec{\boldsymbol{\varphi}}(z_R) \end{pmatrix}_{out} = \boldsymbol{S}\begin{pmatrix} \vec{\boldsymbol{\varphi}}(z_L) \\ \overleftarrow{\boldsymbol{\varphi}}(z_R) \end{pmatrix}_{in} = \begin{pmatrix} \boldsymbol{r} & \boldsymbol{t}' \\ \boldsymbol{t} & \boldsymbol{r}' \end{pmatrix}\begin{pmatrix} \vec{\boldsymbol{\varphi}}(z_L) \\ \overleftarrow{\boldsymbol{\varphi}}(z_R) \end{pmatrix}, \tag{14}$$

where $\boldsymbol{t}$ and $\boldsymbol{r}$ ($\boldsymbol{t}'$ and $\boldsymbol{r}'$) are $(N\times N)$ transmission and reflection amplitudes for left (right) incident particles, one can deduce the well-known relations for the scattering amplitudes[27]

$$\boldsymbol{r} = -\boldsymbol{\delta}^{-1}\boldsymbol{\gamma},$$

$$\boldsymbol{t} = \boldsymbol{\alpha} - \boldsymbol{\beta}\boldsymbol{\delta}^{-1}\boldsymbol{\gamma},$$

$$\boldsymbol{t}' = \boldsymbol{\delta}^{-1},$$

$$\boldsymbol{r}' = \boldsymbol{\beta}\boldsymbol{\delta}^{-1}. \tag{15}$$

These together with Eq. (12) allow the calculation of the relevant physical quantities. Assuming incidence of particles from the left only, the transmission coefficient from channel j to channel i is given by

$$T_{ij} = |t_{ij}|^2. \tag{16}$$

The total transmission probability to channel i (channel conductance in units of $e^2/\pi\hbar$) will be obtained from[19]

$$G_i = \sum_j |t_{ij}|^2. \tag{17}$$

The sum runs over all the incident channels j. Other quantities that will be calculated here are the two-probe Landauer conductance[28] defined, in units of $e^2/\pi\hbar$, as

$$G = \mathrm{Tr}(\boldsymbol{t}\boldsymbol{t}^\dagger), \tag{18}$$

and the transmission phase times[29–32]

$$\tau_{ij} = \frac{\partial \theta_{ij}}{\partial \omega} \tag{19}$$

with θ_{ij} the phase of t_{ij}.[33]

Finally, a few comments on the orthonormal basis and its consequence on the flux conservation requirements and the scattering matrix unitarity. Given the current density written in the EFA models like[34,35]

$$j(z) = -i[\boldsymbol{A}(z)^\dagger \boldsymbol{F}(z) - \boldsymbol{F}(z)^\dagger \boldsymbol{A}(z)], \tag{20}$$

where $\boldsymbol{A}(z)=\boldsymbol{B}(z)\boldsymbol{F}'(z)+\boldsymbol{P}(z)\boldsymbol{F}(z)$ is a linear form from Eq. (3), and using some identities of the QEP, such as Eq. (5c), it is easy to show that the current can be expressed also in the form

$$j(z) = -\sum_{j=1}^{2N} \boldsymbol{c}_j^* \boldsymbol{c}_j = -\boldsymbol{c}^\dagger \boldsymbol{c} = -(\boldsymbol{a}^\dagger \boldsymbol{a} - \boldsymbol{b}^\dagger \boldsymbol{b}). \tag{21}$$

The coefficients $\boldsymbol{a}$, $\boldsymbol{b}$, and $\boldsymbol{c}$ were introduced in Eqs. (2) and (8). This result and the current-conservation requirement leads one, straightforwardly, to obtain the well-known flux conservation condition[27]

$$\boldsymbol{M}_{sv} \boldsymbol{\Sigma}_z \boldsymbol{M}_{sv}^\dagger = \boldsymbol{\Sigma}_z. \tag{22}$$

Here $\boldsymbol{\Sigma}_z=\boldsymbol{I}_2 \otimes \boldsymbol{\sigma}_z$ is the generalized Pauli matrix σ_z. From Eq. (22) it is easy to obtain the cardinal unitarity property (6) of the scattering matrix S. The pseudo-unitarity condition suggested by Sánchez and Proetto[16] for "scattering matrices" is just a particular way of amending the lack of an orthonormal basis [in the sense of Eq. (5)], which, otherwise, leads to a violation of flux conservation. Hereafter $\boldsymbol{O}_\mathrm{N}$ and $\boldsymbol{I}_\mathrm{N}$ stand for the corresponding $(N\times N)$ null and identity matrices.

III. AN EXAMPLE: THE (4×4) KOHN-LUTTINGER MODEL

The KL model, widely used to study the electronic properties in III-V and II-VI semiconductor valence bands, considers in the $\boldsymbol{k}\cdot\boldsymbol{p}$ approximation the highest two valence bands degenerated in the Γ-point of the Brillouin zone. The usual (4×4) Kohn-Luttinger Hamiltonian is of the form

$$\hat{\boldsymbol{H}}_\mathrm{KL} = \begin{pmatrix} H_{11} & H_{12} & H_{13} & 0 \\ H_{12}^* & H_{22} & 0 & -H_{13} \\ H_{13}^* & 0 & H_{22} & H_{12} \\ 0 & -H_{13}^* & H_{12}^* & H_{11} \end{pmatrix}, \tag{23}$$

where

$$H_{11} = A_1 \kappa_\mathrm{T}^2 + V(z) - B_2 \frac{\partial^2}{\partial z^2},$$

$$H_{12} = \frac{\hbar^2\sqrt{3}}{2m_0}[\gamma_2(k_y^2 - k_x^2) + 2i\gamma_3 k_x k_y],$$

$$H_{13} = i\frac{\hbar^2\sqrt{3}}{2m_0}\gamma_3(k_x - ik_y)\frac{\partial}{\partial z},$$

$$H_{22} = A_2 \kappa_\mathrm{T}^2 + V(z) - B_1 \frac{\partial^2}{\partial z^2},$$

with

$$A_1 = \frac{\hbar^2}{2m_0}(\gamma_1 + \gamma_2); \quad A_2 = \frac{\hbar^2}{2m_0}(\gamma_1 - \gamma_2),$$

$$B_1 = \frac{\hbar^2}{2m_0}(\gamma_1 + 2\gamma_2); \quad B_2 = \frac{\hbar^2}{2m_0}(\gamma_1 - 2\gamma_2). \tag{24}$$

In Eq. (23), the atomiclike states, which correspond to the valence band states of interest, are taken as $hh_{+3/2}$, $lh_{-1/2}$, $lh_{+1/2}$, and $hh_{-3/2}$, after Ref. 24. Though in general the precise definition of physical channels depend on the physical problem envisioned, in this model each of the four components of $\boldsymbol{F}_\mathrm{KL}(z)$, corresponding to one of the angular momentum components $m_j=\pm3/2$ and $m_j=\pm1/2$, are the physical channels to deal with. It is worth noticing that each $\boldsymbol{F}_\mathrm{KL}(z)$ component is a linear superposition of right and left moving quasiparticle states.

It is easy to see that, independently of the specific parameters, the matrices $\mathbb{M}$, $\mathbb{C}$, and $\mathbb{K}$ associated to the QEP of $\hat{\boldsymbol{H}}_\mathrm{KL}$ are

$$\mathbb{M}_\mathrm{KL} = \begin{pmatrix} B_2 & 0 & 0 & 0 \\ 0 & B_1 & 0 & 0 \\ 0 & 0 & B_1 & 0 \\ 0 & 0 & 0 & B_2 \end{pmatrix}, \tag{25}$$

$$\mathbb{C}_\mathrm{KL} = \begin{pmatrix} 0 & 0 & \mathcal{H}_{13} & 0 \\ 0 & 0 & 0 & -\mathcal{H}_{13} \\ \mathcal{H}_{13}^* & 0 & 0 & 0 \\ 0 & -\mathcal{H}_{13}^* & 0 & 0 \end{pmatrix}, \tag{26}$$

with $\mathcal{H}_{13}=-\frac{\hbar^2\sqrt{3}}{2m_0}\gamma_3(k_x-ik_y)$, and

$$\mathbb{K}_{\mathrm{KL}} = \begin{pmatrix} A_1\kappa_{\mathrm{T}}^2 + V(z) - E & H_{12} & 0 & 0 \\ H_{12}^* & A_2\kappa_{\mathrm{T}}^2 + V(z) - E & 0 & 0 \\ 0 & 0 & A_2\kappa_{\mathrm{T}}^2 + V(z) - E & H_{12} \\ 0 & 0 & H_{12}^* & A_1\kappa_{\mathrm{T}}^2 + V(z) - E \end{pmatrix}. \tag{27}$$

An important role in our approach is played by the crucial relation (9), which is easily obtained when the envelope function is given in the propagating modes representation and it is written as

$$\boldsymbol{F}_{\mathrm{KL}}(z) = \boldsymbol{\mathcal{N}}_{11}\boldsymbol{a}\tilde{\boldsymbol{\varphi}}(z) + \boldsymbol{\mathcal{N}}_{12}\boldsymbol{b}\tilde{\boldsymbol{\varphi}}(z) \tag{28}$$

with

$$\boldsymbol{\mathcal{N}}_{11} = (\boldsymbol{\psi}_1\boldsymbol{\psi}_2\cdots\boldsymbol{\psi}_4) \tag{29}$$

$$\boldsymbol{\mathcal{N}}_{12} = (\boldsymbol{\psi}_5\boldsymbol{\psi}_6\cdots\boldsymbol{\psi}_8). \tag{30}$$

Therefore, we obtain the fundamental relation

$$\boldsymbol{\psi}_{\mathrm{KL}}(z) = \begin{pmatrix} \boldsymbol{\mathcal{N}}_{11} & \boldsymbol{\mathcal{N}}_{12} \\ i\boldsymbol{\mathcal{N}}_{11}\boldsymbol{Q} & -i\boldsymbol{\mathcal{N}}_{12}\boldsymbol{Q} \end{pmatrix} \begin{pmatrix} \boldsymbol{a} & 0 \\ 0 & \boldsymbol{b} \end{pmatrix} \begin{pmatrix} \tilde{\boldsymbol{\varphi}} \\ \tilde{\boldsymbol{\varphi}} \end{pmatrix} = \boldsymbol{\mathcal{N}}\boldsymbol{\Phi}_{\mathrm{KL}}(z) \tag{31}$$

for the 4×4 KL model. Here we have defined the matrix

$$\boldsymbol{Q} = \begin{pmatrix} q_{hh} & 0 & 0 & 0 \\ 0 & q_{lh} & 0 & 0 \\ 0 & 0 & q_{lh} & 0 \\ 0 & 0 & 0 & q_{hh} \end{pmatrix}$$

containing the QEP eigenvalues. The spinors in Eqs. (29) and (30) are the orthonormalized eigenvectors of the corresponding QEP. The order in which spinors are labeled should be consistent with the labeling of the scattering matrix elements. We are now able to distinguish incoming and outgoing channels, as well as all the possible transitions among them. Given the transformation (31), relating the bulklike plane wave states with well-defined right and left propagating modes, we have the similarity transformation [Eq. (12)].

IV. NUMERICAL RESULTS

To make clear the notation employed here, let us consider again Fig. 1. We sketch there a multichannel hole transport process through a GaAs-cladding layer $(L)/(\mathrm{AlAs/GaAs})^n/$ GaAs-cladding layer (R) heterostructure. As is well-known, the alternation of AlAs and GaAs layers lead to a sequence of valleys and barriers in the conduction and valence bands. For systems with a small number of layers like in the double barrier systems (DBS), or systems with a larger number of layers but locally periodic, the transmission process is resonant and occurs through a number of levels or subbands (where the transmission coefficient is close to one). Within the heterostructure, heavy and light holes (hh and lh) can scatter to any of the energetically possible states. In this section we will refer to direct and crossed transitions processes (dashed and solid arrows, respectively, in Fig. 1). For locally periodic (bicomponent) systems $BABAB\ldots$, with alternating wells B of length L_w and barriers A of length L_b, we consider single cells of the form $B^{1/2}AB^{1/2}$ (with $B^{1/2}$ half layer B), of length $l_c=L_w+L_b$. In all examples considered here, we will have $L_w=50$ Å and L_b (ranging between 10 and 40 Å). The Luttinger parameters are taken after Ref. 36. The incident and transmitted channels are labeled according to Ref. 24. All numerical results presented in this section were obtained for transmission processes along the z-direction (see Fig. 1).

A. Transmission probabilities in the limit of uncoupled modes ($\kappa_T=0$)

In Fig. 2 we show the transmission probabilities for "direct path" processes, i.e., for $hh_{+3/2}\rightarrow hh_{+3/2}$ and $hh_{-3/2}$

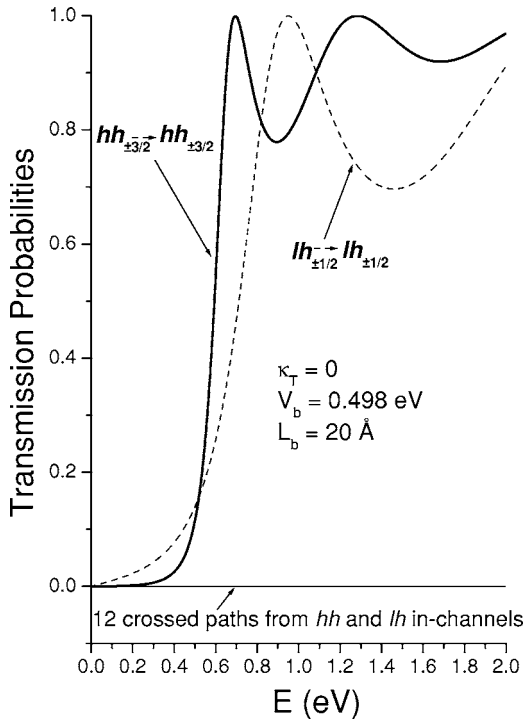

FIG. 2. Transmission probabilities T_{ij} as functions of the incident-particles energy for the heterostructure GaAs-cladding layer $(L)/(\mathrm{AlAs/GaAs})^n/$GaAs-cladding layer (R) when $\kappa_{\mathrm{T}}=0$, $V_b=0.498$ eV, and $n=1$. The solid-thick line curve describes the direct paths $hh_{\pm3/2}\rightarrow hh_{\pm3/2}$, and the broken line $lh_{\pm1/2}\rightarrow lh_{\pm1/2}$. The solid-thin horizontal line represents the 12 crossed paths, which as expected are forbidden.

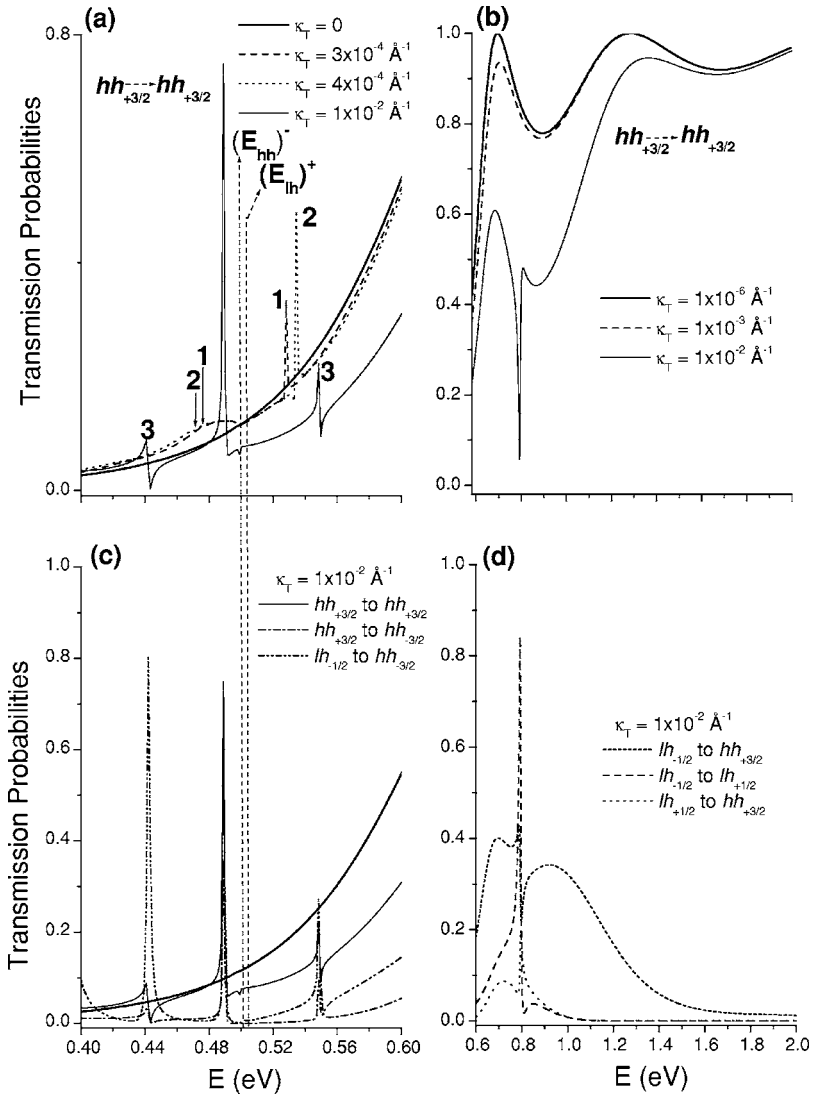

FIG. 3. Transmission coefficients as functions of the incoming energy. Frames (a) and (c) for energies below the barrier and panels (b) and (d) for energies above the barrier. In (a) T_{ii} (with $i=hh_{+3/2}$) for $V_b=0.498$ eV, $n=1$ for several values of κ_T and energies below 0.6 eV. Two vertical dashed lines indicate the reference energy window $(E_{lh})^+$ and $(E_{hh})^-$ at $\kappa_T=0.01$ Å^{-1}. In this panel the spikes 1, 2, and 3 above the energy window are the same transition for three different values of κ_T. (b) T_{ii} (with $i=hh_{+3/2}$) for several values of κ_T and energies above 0.6 eV. It is clear from this panel and (a) that, for energies above the barrier, increasing κ_T the direct-processes transmission coefficient decreases. In (c) we have T_{ij} for the crossed paths $hh_{+3/2} \rightarrow hh_{-3/2}$ and $lh_{-1/2} \rightarrow hh_{-3/2}$ when $\kappa_T=0.01$ Å^{-1}. We show also T_{ii} for $i=hh_{+3/2}$ and two values of κ_T: $\kappa_T=0$ (solid thick) and $\kappa_T=0.01$ Å^{-1} (solid thin). (d) The crossed paths transmission coefficient T_{ij} for $lh_{-1/2} \rightarrow hh_{+3/2}$, $lh_{-1/2} \rightarrow lh_{+1/2}$, and $lh_{+1/2} \rightarrow hh_{+3/2}$. All for the same value of κ_T. At larger energies the crossed paths transmission coefficients drop again to zero.

$\rightarrow hh_{-3/2}$ (solid lines) and $lh_{+1/2} \rightarrow lh_{+1/2}$ and $lh_{-1/2} \rightarrow lh_{-1/2}$ (dashed lines), when $\kappa_T=0$. An interesting but not unexpected result is that uncoupled holes with equal effective mass and opposite angular momentum components m_j have exactly the same tunneling probability, which means that reversing the total angular momentum orientation, the transmission rate remains invariant. Nevertheless, our model is able to solve between the four *in-out* channels, which, in turn, allows one to state that, in the uncoupled limit, the crossed paths $hh_{+3/2} \rightarrow hh_{-3/2}$ and $lh_{+1/2} \rightarrow lh_{-1/2}$ (horizontal line in Fig. 2) are closed in both directions. In this uncoupled-modes limit, the four direct paths are the allowed transmission processes, while the crossed paths are forbidden. It can also be noticed that at low energies, the transition probabilities for light holes is larger than for heavy holes, in agreement to single-band model predictions. This behavior changes in the presence of band mixing.

B. Transmission probabilities for coupled modes $\kappa_T \neq 0$. Strong dependence on κ_T

The coupling effects manifest themselves through an important number of different transmission probability features. We shall refer here only to the most relevant and apparent ones. In Figs. 3(a) and 3(b) we plot the direct process transmission coefficient T_{ii} with $i=hh_{+3/2}$ for several transverse wave numbers, null and non-null. The most visible characteristics in these figures are the gradual transfer of flux from direct to crossed paths at higher energies as κ_T is increased and the strong resonant interference phenomena at low energies. The remarkable reduction in the direct process transmission coefficient contrasts with the increase of crossed processes probability [shown partially in Fig. 3(d)]. For energies below the barrier height ($V_b=0.48$ eV) the evanescent modes couple resonantly with negligible effects on the transport properties. From Fig. 3(d) we notice also that for larger Fermi energies, the crossed-paths transmission coefficients T_{ij} drop to zero and the direct processes become, again, the dominant ones. The constructive interference between channels, in the finite κ_T regime described by the KL model considered here, takes place with different characteristics for energies below and above the potential barrier.

In Sec. IV B 2, we will analyze the meaning of E_{lh}^+ and E_{hh}^-, as well as the relation between the resonant peaks in Figs. 3(a) and 3(c) and the threshold effects.

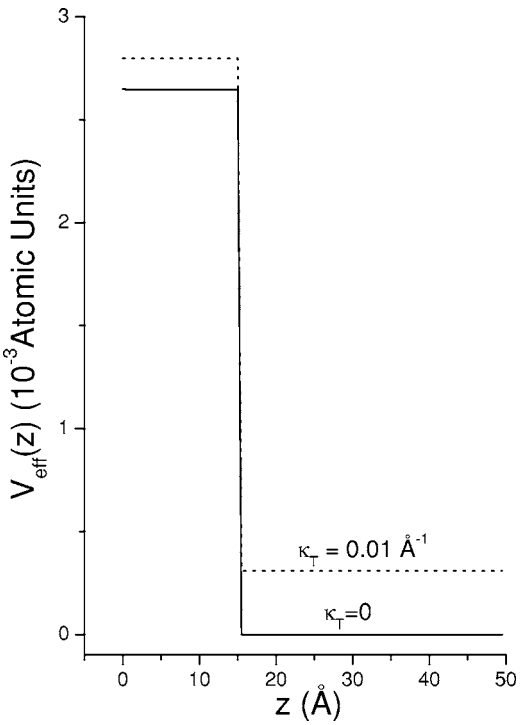

FIG. 4. Qualitative approximation to the potential energy observed by holes for two different values of κ_T. The same potential $V(z)$ is used and the difference appears for the κ_T terms. The calculation was performed for a symmetrical barrier and only one half is plotted.

The similarities observed in the direct transitions from *hh* and *lh* at normal incidence gradually fade as κ_T grows, even at low energies. This is a consequence of the anisotropy and the nonparabolicity, which lead on to an interfering process among channels.

It is important to notice that the potential "observed" by holes during their movement changes as κ_T changes too. To evaluate this effect qualitatively, the following calculation was performed: The matrix $\boldsymbol{W}$, in Eq. (3), includes the potential $V(z)$, the energy eigenvalue, and some terms of the KL Hamiltonian depending on κ_T. Diagonalizing this matrix, one can roughly assert that the "interaction eigenvalues" correspond, in some sense, to an effective potential seen by the heavy and light holes. After performing this type of exercise, we obtain the following results: the barrier height reduces and the band edge moves upward as κ_T increases (see Fig. 4). This figure shows also, that for larger values of κ_T the low energy particles might be below the band edge, leading (within other evanescent-mode interference effects) to a reduction in the transmission probabilities of direct processes. As the model we are using is elastic, that reduction at low energies leads to the opening of crossed-paths in the same energy range as a balance mechanism. For the same reason the opposite occurs at the high energy range in which no strong dependence on κ_T is observed [see panels 3(b) and 3(d)]. On the other hand, the potentials obtained for heavy and light holes are quite similar even though the dependence on κ_T, for each type of hole, is different. In these calculations we used the Luttinger parameters quoted in Ref. 37.

1. Transitions between modes with Kramer-up (+) and Kramer-low (−) sign to time reversal operation

In Ref. 15, sensitive differences in the transmission quantities when comparing the (2×2) u and l subspaces were reported. These differences justify the existence of transitions between them. Figure 3(d) shows the transmission probabilities of the crossed-paths $lh_{-1/2}\rightarrow lh_{+1/2}$ (dashed line) and the $lh_{+1/2}\rightarrow hh_{+3/2}$ (dotted line) whose initial and final states belong to different subspaces, in the sense of the sign of Kramer degeneracy under the time reversal symmetry [a well-defined symmetry within the (4×4) KL model Hamiltonian[17,38]]. Crossed-path transmissions of this kind cannot obviously be observed working separately in the usual (2×2) u and l KL subspaces,[13–16,39] since the Kramer (+) and Kramer (−) propagating modes are not related in the framework of such scheme. Even though we are not asserting that the early studies of these phenomena are wrong when using the (2×2) KL subspaces, we consider that these transitions are naturally absent from their analysis. We guess that the crossed-path resonances will be observed experimentally for high values of κ_T

2. Threshold effect: Evanescent modes contribution to transmission

In the AlAs barrier (layer A, Fig. 1) the longitudinal k_z eigenvalues (denoted as q_{hh} and q_{lh}) can take imaginary, complex, or real values, as reported before.[15,16] In the first two cases, we are in the presence of evanescent modes, which occur basically at low energies. To gain some insight into the rather complicated resonant interference phenomena, let us consider the dispersion relations of the bulk[16] (here $k_z=0$)

$$(E_{hh})^- = R_y a_O^2(\gamma_1 - 2\gamma_2)\kappa_T^2 + V_b$$

$$(E_{lh})^+ = R_y a_O^2(\gamma_1 + 2\gamma_2)\kappa_T^2 + V_b, \qquad (32)$$

which determine a reference energy window defined by $[(E_{lh})^- \lesssim E \lesssim (E_{hh})^+]$, that widens as κ_T increases (see Fig. 5) and closes precisely at $E=V_b=0.5$ eV, when $\kappa_T=0$. Here R_y and a_O stand for the Rydberg constant and the Bohr's radius, respectively. For a fixed transverse momentum κ_T, the resonances of direct and crossed transmission coefficients are correlated, as can be seen in Figs. 3(a) and 3(c) (for $\kappa_T=0.01$ Å^{-1}). As κ_T departs from zero and the energy window opening broadens, the resonant peaks move away from $E=V_b$. In fact the spikes labeled 1, 2, and 3 *above* the energy window in Fig. 3(a) are *the same resonance* for three different values of κ_T (for 3×10^{-4}, 4×10^{-4}, and 1×10^{-2} Å^{-1}, respectively). The same is true for the resonances 1, 2, and 3 *below* the energy window.

Spikes like those shown in Fig. 3(c) have been reported in multichannel electron and hole tunneling.[13,14,22,23,39,40] In this figure, it is important to notice that there is no threshold response effect at $\kappa_T=0$ and no spikes are expected inside

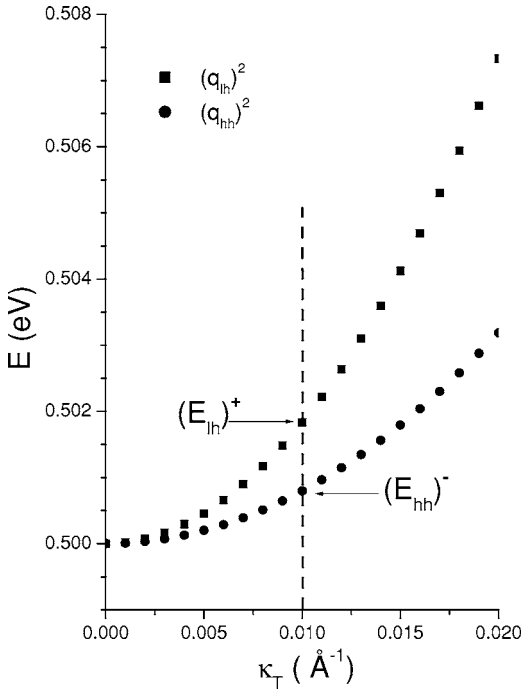

FIG. 5. Broadening of the reference energy window [its limits are defined in Eq. (32)]. The zero-contour curves of the eigenvalues q_{hh} (full circles) and q_{lh} (full rectangles) as a function of κ_T. Here V_b=0.500 eV for AlAs barriers. Below these curves the eigenvalues are purely imaginary (evanescent modes), and above are real (oscillatory modes).

the window. These features emphasize the leading contribution of the evanescent modes to holes transmission processes, via the appearance of spikes during threshold response.

C. Partial conductance, Landauer conductance, and exponential growth of the phase time at κ_T=0

In this section we shall present and discuss results related to the total transmission probability to channel i, G_i, defined in Eq. (17), the conductance G defined in Eq. (18), and the dependence of the phase time with the barrier width. We will analyze basically the barrier width and coherence effects in the uncoupled channels limit κ_T=0, for locally periodic structures. Some calculations have been carried out also for local periodic structures in the interacting modes regime. For the sake of space and clarity we will present only a brief discussion of this case.

1. Barrier width and low energy conductance behavior

In Figs. 6(a) and 6(b) we present the direct process transmission coefficients T_{ii} (for $i=hh_{+3/2}$ and $i=lh_{-1/2}$, respectively) in the uncoupled regime as a function of the incoming energy and barrier width L_b. It can be seen that when the energy is less than V_b the transmission coefficients T_{ii} decrease as L_b increases. Conductance variations are reflected in the curves displayed in the upper part of Fig. 7 for κ_T =0 and L_b=10–40 Å. For $E<V_b$ we observe the same behavior for G as for T_{ii}. However, for $E>V_b$ the resonances of

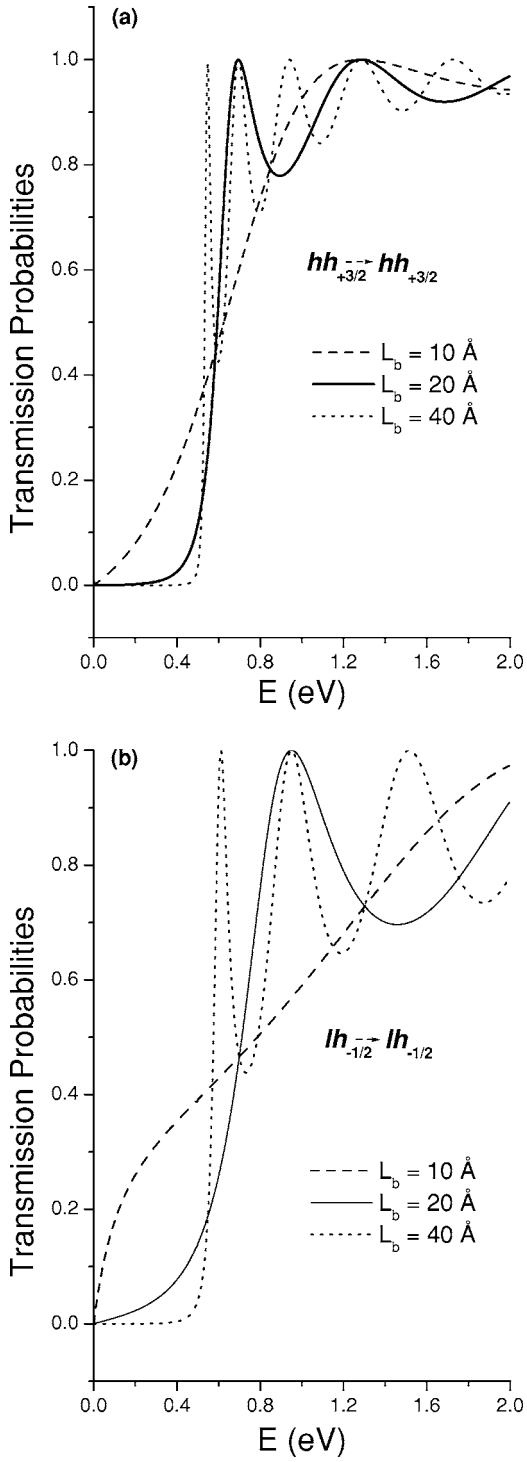

FIG. 6. Transmission probabilities for the direct paths $hh_{+3/2} \rightarrow hh_{+3/2}$ (a) and $lh_{-1/2} \rightarrow lh_{-1/2}$ (b) as functions of the incident particle energy for several values of the barrier thickness. Here κ_T=0, V_b=0.498 eV, and n=1. The resonances move to lower energies and become thinner as L_b increases.

G shift to lower energies while the peaks decrease their intensities differently with what was found for T_{ii}. We guess that for $E>V_b$ in the uncoupled-modes regime, the barrier width is a parameter for the activation of the interference between channels. This strong dependence of the transmis-

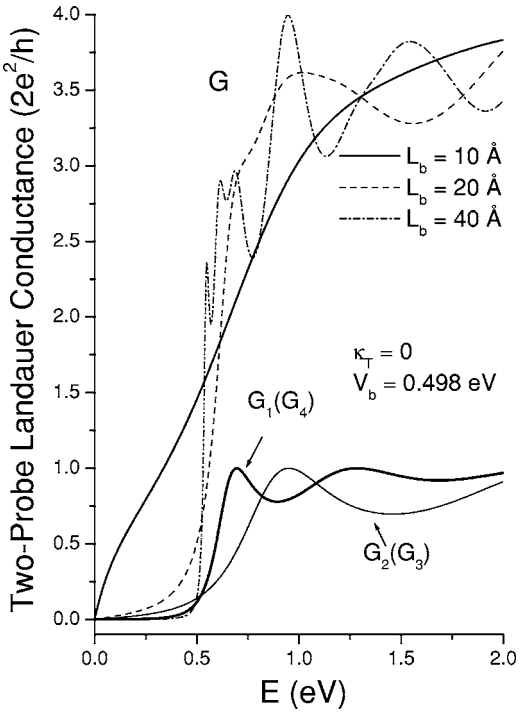

FIG. 7. Partial hole conductances as a functions of the incident energy. Here $\kappa_T=0$, $V_b=0.498$ eV, $L_b=20$ Å, and $n=1$. Solid thick lines show the partial conductance G_1 (G_4) to channel $hh_{+3/2}$ $(hh_{-3/2})$ and the solid thin lines the partial conductance G_2 (G_3) to channel $lh_{-1/2}(lh_{+1/2})$. The two-probe Landauer conductance G is also shown as a function of the barrier width.

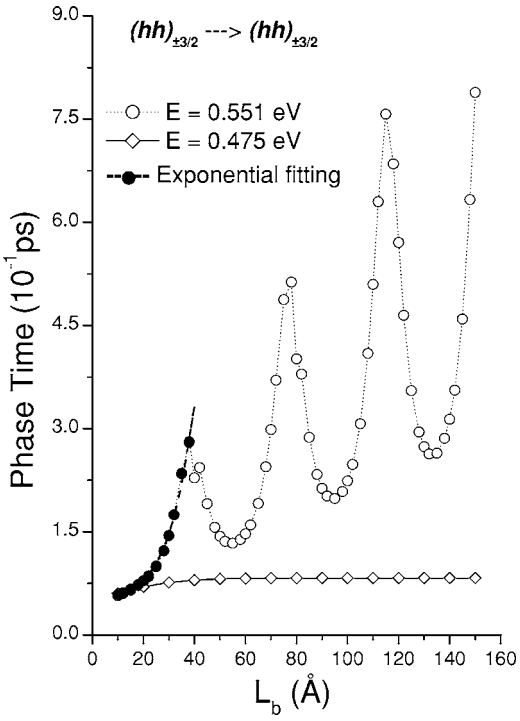

FIG. 8. Phase time vs barrier width for the direct transitions $hh_{\pm 3/2}\rightarrow hh_{\pm 3/2}$ (solid triangles) and an exponential fitting (dashed line) at $E=0.551$ eV.

sion on the barrier width can be used to set the threshold energy in the response of optoelectronics devices in a similar way to what is pursued with the hole absorbtion increment in semiconductor optical amplifiers for the reduction of the current threshold.[10]

2. Homogeneity in the partial conductance of holes

In Fig. 7 we plotted also the total transmission probabilities G_i (referred to also as partial conductance to channel i), as functions of the energy for several values of L_b and for $\kappa_T=0$. It can be noticed that the partial conductances for holes with the same effective mass are equal. The $lh_{\pm 1/2}$ modes open first and provide the main contribution to G_i (and G) at low energies. Comparing the four G_i curves, it is easy to see that the transmitted wave is more or less homogeneously distributed between different outgoing channels. The physical interpretation is the following: The hole tunneling through a single barrier in a multiband-multichannel problem of 4-mixed components, described with the (4×4) KL model for a flatband case, is a balanced phenomenon. The system does not grant any advantage either of the Kramer-*up* or the Kramer-*low* subspaces while it scatters the incoming hole stream. This homogeneous process, in a sense, is a consequence of the time reversal symmetry that the (4×4) KL model fulfills.[17,38] This calculation was done in the framework of an elastic model, then the variations of G for each energy value must be appropriately included in the reflection wave and must be reflected in the charge conservation law. We have successfully evaluated the flux conservation symmetry requirement (22) numerically to confirm its fulfillment—within the machine uncertainty—in a wide range of energies and values of κ_T in the neighborhood of the Γ point.

3. Transmission isotropy

We have not observed remarkable differences in the T_{ij} as well as in other transmission quantities while changing the in-plane direction along $\langle 10\rangle$ to $\langle 11\rangle$, for different values of the transversal quasimomentum. This isotropy of hole quantum transport described by the KL model used here, contrasts with the well-known strong anisotropy of the valence band of layered heterostructures of III-V materials.[16,24,38]

4. Barrier width and phase time of holes

In Ref. 41 an exponential growth of the phase time with the barrier width was reported for electrons, with energies above the barrier. For holes, to our knowledge, there are neither theoretical nor experimental reports of such a dependence. For energies below the barrier the hole tunneling time is consistent with Hartman effect. For energies above the barrier the transit time oscillates and increases steadily with L_b. Only in the small-barrier-width region the transit time grows exponentially with L_b. In Fig. 8 we show the barrier width dependence of the phase time for the direct $hh_{\pm 3/2}\rightarrow hh_{\pm 3/2}$ transition together with a fitting using an exponential function. The details of this calculation and its analysis are in progress and will be published elsewhere.

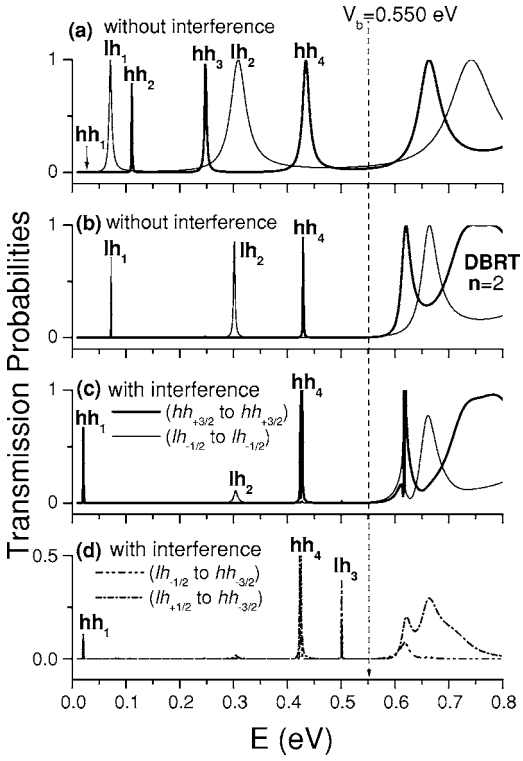

FIG. 9. Discrete quasistationary bound levels in a 50 Å GaAs quantum well within the DBRT GaAs-cladding layer $(L)/(\mathrm{AlAs/GaAs})^2$/GaAs-cladding layer (R). For $E<V_b$, Fano-type transmission resonances of *hh* and *lh* through the double barrier resonant tunneling system with AlAs barriers. In panel (a) $\kappa_T=0$ and $L_b=10$ Å. In (b) the same as in panel (a) but $L_b=20$ Å. In (c) and (d) $\kappa_T=0.01$ Å^{-1} for $L_b=10$ Å and $L_b=20$ Å, respectively. In all cases, unbound hole levels are evident for $E>V_b$ and they displace to lower energies with barriers broadening, as expected.

D. Spectral quantities in multilayer systems

We will consider here heavy- and light-holes band structures from the point of view of the multicomponent scattering approach. The results obtained here agree with the well-known transmission-coefficients band structure of finite periodic systems (characterized by a finite number of intraband energy levels[23]), at variance with the continuous band structures predicted for infinite periodic systems.

1. Discrete quasistationary levels in a DBRT

In Figs. 9(a)–9(c) we plot several transmission coefficients T_{ij} for a double barrier resonant tunneling (DBRT) system, with i and j as indicated in each panel. Specifically we consider the heterostructure GaAs-cladding layer $(L)/(\mathrm{AlAs/GaAs})^n$/GaAs-cladding layer (R) with $n=2$. At low energies, $E<V_b$, discrete quasistationary hole levels in the quantum well of the DBRT heterostructure[7,9,12,15,16,42] are correctly resolved into sharp individual resonances. The quasistationary levels are the same for all panels in Fig. 9. Zero transmission in multiband systems[43] occurs in between isolated Fano resonances[44] when a bound state in the well is coupled to states in the continuum. Previous works report Fano resonances for *lh* in tight-binding $sp3s^*$ calculations, in which, even at $\kappa_T=0$, the bands *lh*, *hh* and spin split are coupled by symmetry breaking and spin-orbit interaction.[45] In Fig. 9, panels (a) and (b), we show isolated Fano resonances for *hh* and *lh* bands. In the uncoupled channels limit[46] only the quasistationary states hh_j with $j=1,2,3,4$ contribute to T_{ii} with $i=hh_{+3/2}$ (thick solid line), while the main contributions to T_{ii} for $i=lh_{-1/2}$ (thin solid line) come from the quasistationary light hole states lh_1 and lh_2.

In the uncoupled regime, the Hamiltonian $\hat{\boldsymbol{H}}_{\mathrm{KL}}$ in Eq. (23) is diagonal, hence an independent band approximation is possible. The *hh* states must be closer to one another due to their greater effective mass. This is reflected in thinner resonance peaks of heavy hole states in panels (a) and (b) of Fig. 9. In (a) the barriers for *hh* are more opaque than for *lh*, therefore, the *hh* are strongly confined with larger lifetimes. The widths of hh_j peaks with $j=1,2,3,4$ are 1.8, 2, 5, and 15 meV, respectively, while for the lh_j peaks with $j=1,2$ are 34 and 67 meV.

For $\kappa_T\neq 0$ we find strong band coupling with interfering effects absent in the actual one component approaches. In panel (c) of Fig. 9 we have the transmission coefficients for the same direct paths as in panel (a). One of the most interesting results is the probability that a charge carrier incident as a *hh* or *lh* state emerges on the other side as a different quasiparticle.[23,42] In panel (d) of Fig. 9, we see that for such crossed-transition paths the charge carrier resonates with energy levels of the inner well having the same or different effective mass. For example, the crossed path $lh_{-1/2}\rightarrow hh_{-3/2}$ (double dotted dashed line) which involves a change in effective mass and in Kramer sign, is resonant at $E=0.0204$ eV corresponding to a hh_1 state, and at $E=0.5009$ eV through the lh_3 state. For the crossed-path $lh_{+1/2}\rightarrow hh_{-3/2}$ (short dashed-dotted line), where only the effective mass changes while the Kramer sign is kept constant, the incident light hole resonates at $E=0.5009$ eV, with a light hole state lh_3 to come out as a heavy hole state. It is important to highlight that the state lh_3 is seen only through crossed-paths and does not appear at $\kappa_T=0$ [in panels (a) and (b) of Fig. 9]. The constraints imposed to the incident flux could be the reason why this state does not appear in previous reports[12,46] using similar parameters.

Figure 10 shows theoretical and experimental quasistationary levels of the inner well in a double barrier system. The experimental results from a typical resonant-tunneling diode are displayed with symbols.[40] Numerical calculations obtained by means of transmission coefficient resonances (dashed thin/thick lines), reported by other authors, are shown together with our results. The agreement between our results and the experiment is rather good.

2. Band structure and superlattices

The purpose of the sequence of plots in Fig. 11 is to illustrate the formation of the heavy-hole and light-hole band structures as the number of cells n grows.[23] In Fig. 11(a) the heavy-hole resonance splits and a band structure emerges. In the case of heavy holes the band spectrum reveals itself reasonably well defined, already for n of the order of 5. It is worth noticing that, even though the band structure is a consequence of and will emerge once the phase coherence and

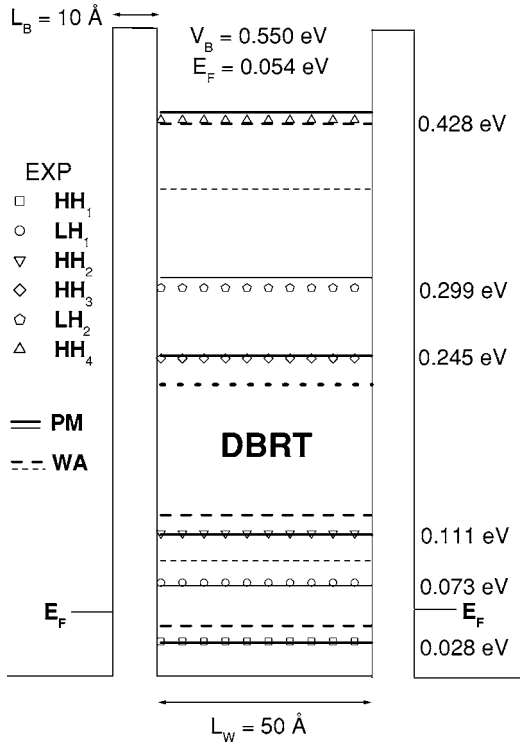

FIG. 10. Schematic representation of the energy levels of quasistationary states in the inner well of a DBRT structure. The experimental results given in Ref. 40 (for *hh* and for *lh*) are shown with symbols. WA stands here for the theoretical results reported in Ref. 12 (dashed lines). PM stands for the present method results (solid lines). Here we use thin lines for *hh* levels and thick lines for *lh* levels. The numbers on the right-hand side are the experimental values. E_F indicates the Fermi level.

the periodicity have been combined, the single-cell multichannel-multiband transfer matrix $\boldsymbol{M}_{sy}$ already contains information of this fundamental property[23,47] (see Fig. 2). Additional calculations are in progress for locally periodic systems and related physical quantities, such as the phase time.

V. CONCLUSIONS

An approach that is able to resolve the multimode transport processes was developed. This approach is based on the standard multiband Hamiltonians, the quadratic eigenvalue problem method, and the multichannel transfer matrix techniques. We applied this approach to study transmission of holes described by a multiband-multichannel model. In this approach we do not need to impose any restriction on the incident flux of holes, i.e., we study all amplitudes of heavy and light holes at the same time. Without disproving the input assumptions used in Refs. 11–15, in accordance with the general remarks of quantum mechanics, we can stress that our approach has the benefit of identifying clearly inter- and intra-band hole transitions, and even transitions between states with different Kramer sign to time reversal, which is not the usual case. Moreover, it allows the precise determination of the contribution from each input channel to the

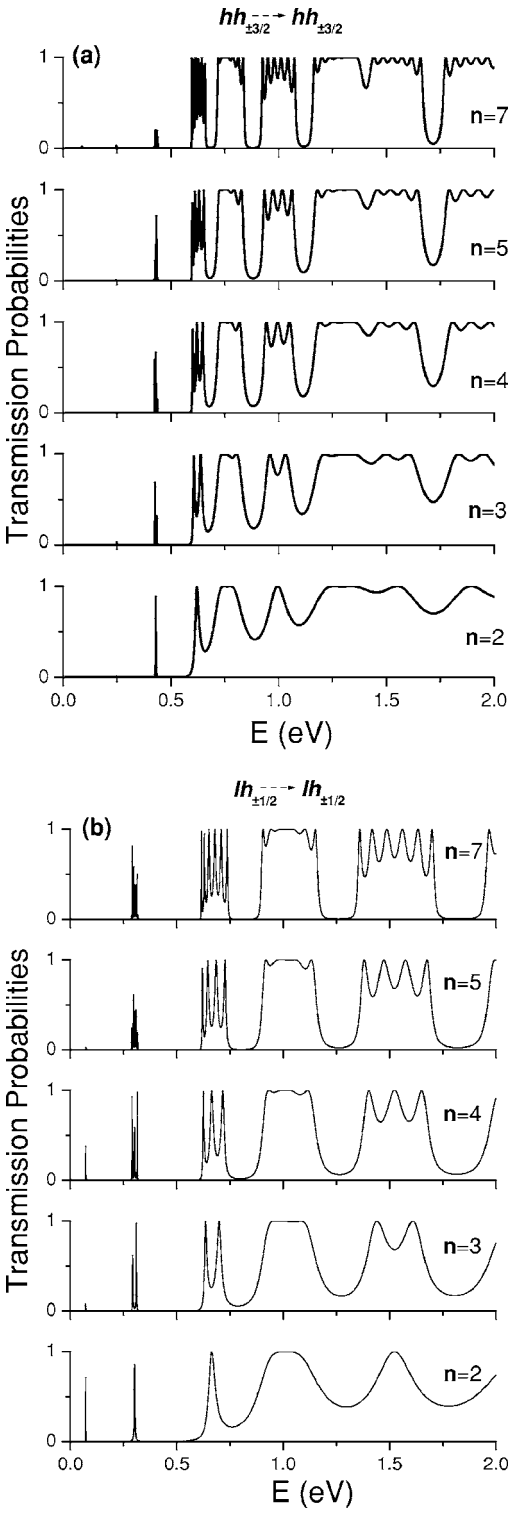

FIG. 11. (a) The metamorphosis of the band spectrum profile for the *hh* bands at $\kappa_T=0$ as a function of the incoming particle's energy and the number of cells. (b) The same as in (a) for the *lh* bands. The single cell dimension was taken as 60 Å for a fixed well thickness of $L_w=50$ Å.

scattering process, boosted by the simultaneous presence of the rest of the channels, which are, in principle, equally accessible to the incident hole stream. We believe that this approach provides more realistic predictions and will be use-

ful in describing forthcoming experiments. The analysis presented here shows that the transmission probabilities are sensible to the transverse wave number κ_T and the geometrical parameters, like the barrier width.

Our approach puts forward the outstanding effect of the evanescent modes to the transmission mechanism and reveals explicitly the band spectrum profile metamorphosis. Channel interference and threshold effects, interposed by bond and evanescent states, are clearly foreseen. The location of the quasistationary states of the well in the DBRT case are in good agreement with typical hole tunneling experiments.

ACKNOWLEDGMENTS

This work was developed under Grant No. E120.1717 of CONACyT of Mexico and partially supported by the Departamento de Ciencias Básicas, UAM-A, Mexico, by the Cátedra de Ciencia Contemporánea, Universitat "Jaume I," Spain and also by the CYTED network IX.E of the CYTED Program of Microelectronics. The authors gratefully acknowledge A. Robledo, J. Gravinsky, V. Velasco, and A. Anzaldo-Meneses for useful and clarifying comments.

*Electronic address: ldiago@fisica.uh.cu
†Electronic address: ppereyra@correo.azc.uam.mx

[1] H. Schneider, H. T. Grahn, K. Klitzing, and K. Ploog, Phys. Rev. B **40**, 10040 (1989).
[2] M. C. Payne, J. Phys. C **19**, 1145 (1986).
[3] W. R. Frensley, Phys. Rev. B **36**, 1570 (1987).
[4] P. Weetman and M. S. Wartaka, J. Appl. Phys. **93**, 9562 (2003).
[5] E. O. Kane, *Tunneling Phenomena in Solids* (Plenum, New York, 1969), Chap. 1.
[6] Y. Ando and T. Itoh, J. Appl. Phys. **61**, 1497 (1987).
[7] M. Morifuji and C. Hamaguchi, Phys. Rev. B **52**, 14131 (1995).
[8] E. O. Kane, *Semiconductors and Semimetals* (Academic, New York, 1966), Vol. 1, p. 75.
[9] M. U. Erdogan, K. W. Kim, and M. A. Stroscio, Appl. Phys. Lett. **62**, 1423 (1993).
[10] A. di Carlo, A. Reale, L. Tocca, and P. Lugli, IEEE J. Quantum Electron. **34**, 1730 (1998).
[11] S. L. Chuang, Phys. Rev. B **40**, 10379 (1989).
[12] R. Wessel and M. Altarelli, Phys. Rev. B **39**, 12802 (1989).
[13] Calvin Yi-Ping Chao and S. L. Chuang, Phys. Rev. B **43**, 7027 (1991).
[14] J. B. Xia, Phys. Rev. B **38**, 8365 (1988).
[15] T. Kumar, M. Cahay, and K. Roenker, Phys. Rev. B **56**, 4836 (1997).
[16] A. D. Sánchez and C. R. Proetto, J. Phys.: Condens. Matter **7**, 2059 (1995).
[17] L. Diago-Cisneros, H. Rodríguez-Coppola, R. Pérez-Alvarez, and P. Pereyra, Phys. Scr. **71**, 582 (2005).
[18] P. Pereyra, J. Math. Phys. **36**, 3 (1995).
[19] P. Pereyra, J. Phys. A **31**, 4521 (1998).
[20] A. Anzaldo-Meneses and P. Pereyra, J. Phys. A (to be published).
[21] F. Tisseur and K. Meerbergen, SIAM Rev. **43**, 235 (2001).
[22] A. Anzaldo, Ann. Phys. **7**, 307 (1998).
[23] P. Pereyra and E. Castillo, Phys. Rev. B **65**, 205120 (2002).
[24] D. A. Broido and L. J. Sham, Phys. Rev. B **31**, 888 (1985).
[25] D. Dragoman and M. Dragoman, J. Appl. Phys. **93**, 6133 (2003).
[26] Systems of the so-called *symplectic universality class*.
[27] P. A. Mello, P. Pereyra, and N. Kumar, Ann. Phys. (N.Y.) **181**, 290 (1988).
[28] R. Landauer, J. Phys.: Condens. Matter **1**, 8099 (1989).
[29] E. P. Wigner, Phys. Rev. **98**, 145 (1955).
[30] E. H. Hauge and J. A. Støvneng, Rev. Mod. Phys. **61**, 917 (1989).
[31] P. Pereyra, Phys. Rev. Lett. **80**, 2677 (1998).
[32] P. Pereyra, Phys. Rev. Lett. **84**, 1772 (2000).
[33] The evaluation of transmission phase and tunneling phase time is underway and will be published elsewhere.
[34] A. M. Malik, M. J. Godfrey, and P. Dawson, Phys. Rev. B **59**, 2861 (1999).
[35] R. Pérez-Alvarez, C. Trallero-Herrero, and F. García-Moliner, Eur. J. Phys. **22**, 275 (2001).
[36] L. R. Ram-Mohan, K. H. Yoo, and R. L. Aggarwal, Phys. Rev. B **38**, 6151 (1988).
[37] I. Vurgaftmana, J. R. Meyer, and L. R. Ram-Mohan, J. Appl. Phys. **89**, 5815 (2001).
[38] L. C. Andreani, A. Pasquarello, and F. Bassani, Phys. Rev. B **36**, 5887 (1987).
[39] D. Z.-Y. Ting, E. T. Yu, and T. C. McGill, Phys. Rev. B **45**, 3583 (1992).
[40] E. E. Mendez, W. I. Wang, B. Rico, and L. Esaki, Appl. Phys. Lett. **47**, 415 (1985).
[41] A. P. Heberle, X. Q. Zhou, A. Tackeuchi, W. W. Rühle, and K. Köhler, Semicond. Sci. Technol. **9**, 519 (1994).
[42] K. V. Rosseau, K. L. Wang, and J. N. Schulman, Superlattices Microstruct. **6**, 67 (1989).
[43] S. Ekbote, M. Cahay, and K. Roenker, Phys. Rev. B **58**, 16315 (1998).
[44] U. Fano, Phys. Rev. **124**, 1866 (1961).
[45] G. Klicmeck, R. Ch. Bowen, and T. B. Boykin, Superlattices Microstruct. **29**, 187 (2001).
[46] Y. X. Liu, D. Z.-Y. Ting, and T. C. McGill, Phys. Rev. B **54**, 5675 (1996).
[47] L. Diago-Cisneros, P. Pereyra, R. Pérez-Álvarez, and H. Rodríguez-Coppola, Phys. Status Solidi B **1**, 125 (2002).